THE JOURNAL OF PHYSICAL CHEMISTRY C
A JOURNAL OF THE AMERICAN CHEMICAL SOCIETY

Open Access
This article is licensed under CC-BY 4.0

pubs.acs.org/JPCC
Article

Co-Sintering Reaction Analysis of NASICON-Type Oxide-Based Solid Electrolyte $Li_{1.3}Al_{0.3}Ti_{1.7}(PO_4)_3$ and Olivine-Type Lithium Metal Phosphates

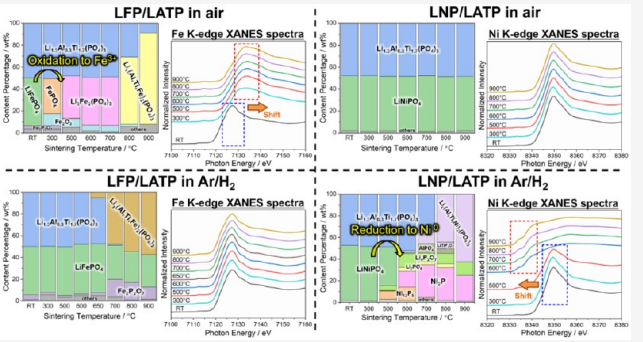
Shuhei Kobayashi, Kei Kubota, Fumihiko Ichihara, Machiko Ode, Shogo Miyoshi, and Takuya Masuda*

Cite This: J. Phys. Chem. C 2026, 130, 12864−12874

Read Online

ACCESS | Metrics & More | Article Recommendations | Supporting Information

ABSTRACT: Composites of a NASICON-type oxide-based solid electrolyte $Li_{1.3}Al_{0.3}Ti_{1.7}(PO_4)_3$ (LATP) and an olivine-type lithium metal phosphate, $LiFePO_4$ (LFP) or $LiNiPO_4$ (LNP), were cosintered at various temperatures in air and an Ar/H_2 atmosphere, and the reaction products were analyzed by X-ray diffraction (XRD), X-ray absorption fine structure (XAFS), and energy-dispersive X-ray spectroscopy (EDS). When the LFP/LATP composites were cosintered in air, LFP oxidized to produce Fe^{3+} compounds such as Fe_2O_3, $FePO_4$ and $Li_3Fe_2(PO_4)_3$, and furthermore, at 800−900 °C, the products further reacted with LATP to form a solid solution denoted as Fe-rich $Li_x(Al,Ti,Fe)_2(PO_4)_3$. On the other hand, in an Ar/H_2 atmosphere, LFP and LATP retained the original olivine and NASICON-type structures up to 600 °C, but at 650 °C or higher, part of the LFP reacted with LATP to form $Fe_2P_2O_7$ and Fe-poor $Li_y(Al,Ti,Fe)_2(PO_4)_3$. In contrast, LNP/LATP composites remained unchanged throughout the temperature range in air, whereas they underwent drastic changes in an Ar/H_2 atmosphere. $Ni_{12}P_5$ and a few minor species such as Ni_2P, $Li_4P_2O_7$ and Li_3PO_4 were produced at 500 °C, Ni_2P, $Li_4P_2O_7$ and Li_3PO_4 became more prominent at 600 °C, and various other phases including $Li_z(Al,Ti,Ni)_2(PO_4)_3$, which could not be fully identified by XRD and XAFS, were formed. In addition, thermodynamic calculations were performed to predict the reaction products. The results showed partial agreement with the experimental observations, and the remaining discrepancies can be attributed to (1) the absence of the thermodynamic parameters of some products in the database used for the calculations, (2) the marginal energy differences between the predicted most stable and the kinetically hindered metastable phases, and (3) the insufficient consideration of the release and uptake of gaseous components including water, oxygen, and hydrogen.



1. INTRODUCTION

Conventional liquid-type lithium-ion batteries (LIBs) using organic liquid electrolytes have been a major power source used in portable devices, electric vehicles and energy storage systems. However, all-solid-state (ASS) LIBs using nonflammable oxide-based solid electrolytes attract much attention because of their excellent safety, lifetime, and reliability, as well as their potentially rapid charge/discharge capability.[1] For the practical implementation of solid-state batteries, it is strongly desired not only to develop a solid electrolyte with excellent ionic conductivity, but also to establish a method for forming highly ion-conductive solid electrolyte/electrode interfaces while preserving their original crystal structures and physical properties.

Co-sintering at high temperatures is a widely used technique to join electrode materials and oxide-based solid electrolytes; however, it often causes undesired side reactions, which can lead to the decomposition of their original crystal structures and excellent ion-conducting properties, or to the formation of a highly ionically insulating layer.[2] Thus, understanding the reaction products from given combinations of substances at given sintering conditions is very important not only for fundamental science but also for designing rational manufacturing processes to form well-defined interfaces.

In this context, reaction products formed by cosintering of electrode materials and solid electrolytes have been analyzed by a few groups.[3−5] Beaupain et al. analyzed the reaction products formed in mixed composites of a NASICON-type solid electrolyte $Li_{1.3}Al_{0.3}Ti_{1.7}(PO_4)_3$ (LATP) and a typical positive electrode material $LiNi_{0.6}Co_{0.2}Mn_{0.2}O_2$ (NCM622) after sintering at various temperatures. They found that even at

Received: June 6, 2026
Revised: August 19, 2026
Accepted: August 20, 2026
Published: September 1, 2026



ACS Publications
© 2026 The Authors. Published by American Chemical Society

https://doi.org/10.1021/acs.jpcc.6c03720
J. Phys. Chem. C 2026, 130, 12864−12874

Downloaded from pubs.acs.org/jpccck/article-pdf/130/37/12864/6809563/acs.jpcc.6c03720.pdf by NATL INST FOR MATLS SCIENCE (NIMS) user on 25 September 2026

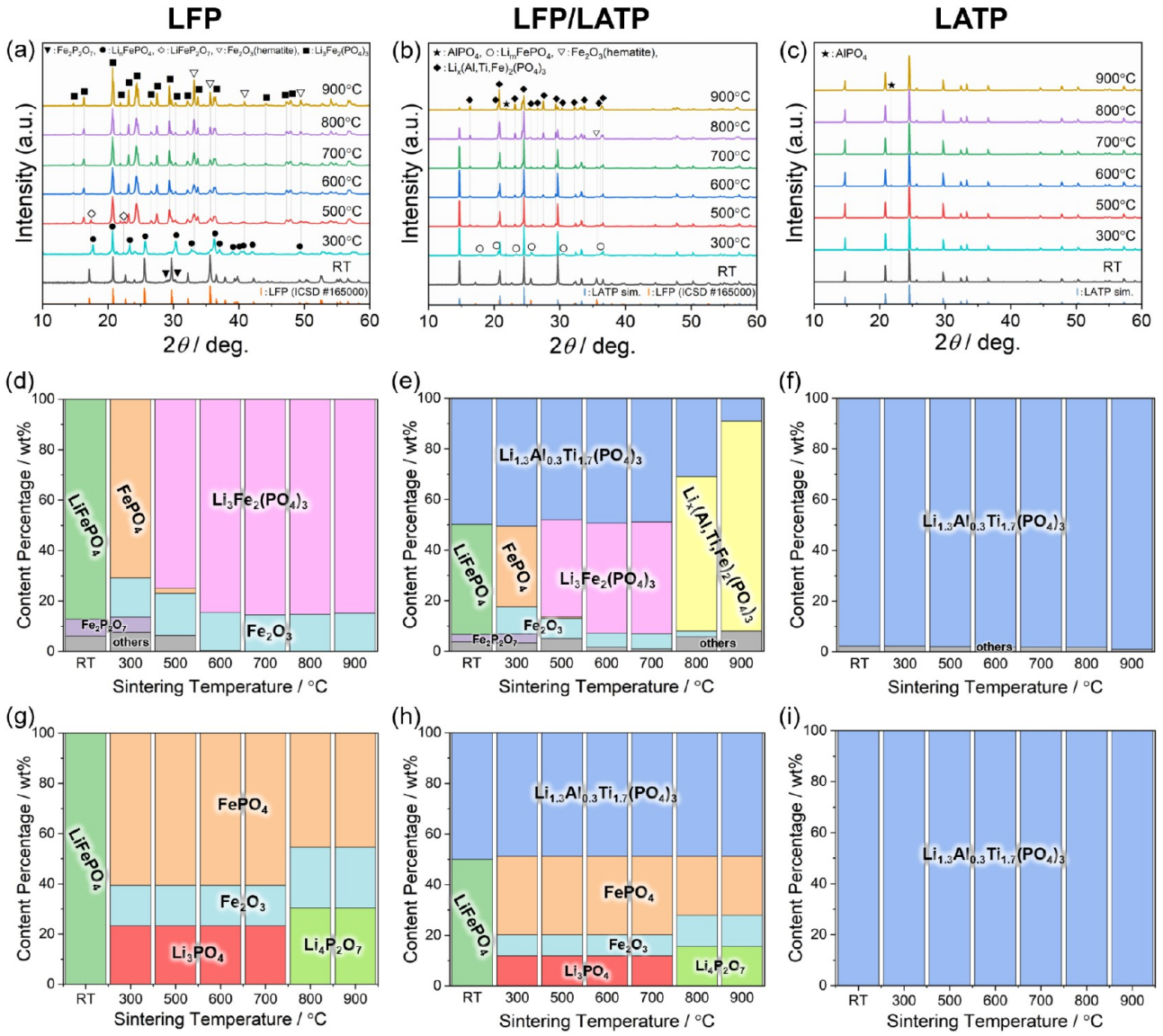


Figure 1. (a–c) XRD patterns and (d–f) phase composition diagrams obtained by Rietveld analysis of (a, d) LFP, (b, e) LFP/LATP and (c, f) LATP sintered at various temperatures in air. Stable phases predicted by thermodynamic calculations of (g) LFP, (h) LFP/LATP and (i) LATP at various temperatures in air.

low sintering temperatures (550–650 °C), NCM622 decomposed into Li_2O and metal oxides such as M_3O_4 and MO (M = Mn, Co, Ni), accompanied by the release of O_2. Subsequently, LATP underwent decomposition to form Li_3PO_4, $LiTiOPO_4$ and TiO_2.[6] Recently, we cosintered LATP and $LiCoO_2$ at various temperatures in air, and comprehensively analyzed the reaction products including crystalline and amorphous substances using a complementary approach integrated with X-ray diffraction (XRD) and X-ray absorption fine structure (XAFS).[5,7] We also applied the macro- and microscopic structural analyses to composites of an olivine-type lithium cobalt phosphate $LiCoPO_4$ (LCP), and LATP sintered at various temperatures in air, and found that LCP and LATP were bound to each other with a thin amorphous interlayer composed of Li_3PO_4 and CoO, which act as an ionic conductor and a sintering additive, respectively.[8]

A variety of important control factors, such as the combinations and compositions of substances, sintering temperatures, and surrounding atmosphere, significantly affect the reaction products. Thus, it is essential to develop a reliable tool which enables us to predict the reaction products for given systems and even propose the optimized sintering condition to form well-defined interfaces among the tremendous combinations of parameters. Thermodynamic calculation is a powerful technique for predicting the thermodynamically stable phases of multicomponent systems under given conditions.[9,10] However, the calculated results, which predict stable phases at infinite time, are not always in full agreement with the products obtained by sintering for a finite duration.[7] Recently, we have compared the experimentally identified reaction products with the stable phases predicted by thermodynamic calculation, to clarify the cause of these discrepancies and improve the accuracy of predictions.[7,11] In the present study, we cosintered LATP together with olivine-type cathode materials such as $LiFePO_4$ (LFP) and $LiNiPO_4$ (LNP) at various temperatures and atmospheres, and quantitatively analyzed the reaction products under each condition with

https://doi.org/10.1021/acs.jpcc.6c03720
J. Phys. Chem. C 2026, 130, 12864–12874

Downloaded from pubs.acs.org/jpccck/article-pdf/130/37/12864/6809563/acs.jpcc.6c03720.pdf by NATL INST FOR MATLS SCIENCE (NIMS) user on 25 September 2026

the aim of understanding the reaction and validation of thermodynamically predicted phases.

2. EXPERIMENTAL METHODS

2.1. Preparation of Sample

LATP, LFP, and LNP powders shown in Figure S1 from Toshima Manufacturing and boron nitride powder from Fujifilm Wako Pure Chemical were used as received. In addition to pure LATP, LFP, and LNP powders, mixtures of LFP and LATP a weight ratio of 1:1 (a molar ratio of 0.709:0.291) and LNP and LATP (a molar ratio of 0.705:0.295) were prepared. The required amounts of each powder were weighed and mixed thoroughly in a zirconia mortar and pestle under dry conditions for 1 h to ensure uniformity. The resulting mixed powders were pressed in an uniaxial die with a diameter of 10 mm at 16 kN for 1 min to form pellets. The formed pellets were placed in alumina crucibles on a bed of powder of the same composition as the pellet, ensuring that each pellet was completely covered. Sintering was carried out in air using a muffle furnace (for static air atmosphere), and under Ar/H_2 (Ar: 95%, H_2: 5%) using a tube furnace with continuous gas flow, at various temperatures from 300 to 900 °C for 8 h. Prior to heating under the Ar/H_2 atmosphere, the furnace containing the samples was purged with the gas mixture for 2 h to eliminate any residual oxygen. The heating and cooling rates were set at 5 °C per minute. It should be noted that atmospheric sintering was conducted using a muffle furnace; therefore, the effects of humidity and CO_2 were not considered in this study. One may concern that LATP, despite its excellent stability for oxidation, is susceptible to reduction and could be reduced during sintering under an Ar/H_2 atmosphere. However, in this study, even when LATP was heated in an Ar/H_2 atmosphere, the only observed change was a grayish discoloration. This was likely caused by the carbonization of organic molecules remaining on the surface from the synthesis stage, and the characteristic blue color associated with reduction did not appear.

2.2. X-ray Diffraction Measurements

XRD measurements were carried out in a Rigaku SmartLab equipped with a Cu Kα source ($\lambda\alpha 1$ = 1.5405 Å) and a two-dimensional detector (Hypix-3000/Rigaku Co., Ltd.). Data were collected in step scan mode with a step width of 0.0028−0.02° and an acquisition time of 1−4°/s. The sintered pellets were pulverized and resulting powder was packed into a nonreflective sample holder for measurement. PDXL2 software (Rigaku, Japan) was used to perform the Rietveld analysis. Table S1 and Figures S2−S11 in the Supporting Information show the input powder diffraction files for Rietveld analysis from the international center for diffraction data (ICDD) and the results of Rietveld analysis, respectively.

2.3. X-ray Absorption Spectroscopy Measurements

XAFS measurements at the Ti, Fe, and Ni K-edges were carried out in transmission mode at BL9A and BL9C equipped with Si(111) double crystal monochromators at the Photon Factory (PF), High Energy Accelerator Research Organization (KEK) in Tsukuba, Japan.[12,13] The ring energy was 2.5 GeV and the maximum current was 450.0 mA. The X-ray photon energy was calibrated using Ti, Fe, and Ni metal foils as standard samples. Data processing, including background subtraction, was performed using the ATHENA program.[14] The sintered pellets were pulverized, diluted with boron nitride powder, and remolded into pellets.

2.4. Scanning Electron Microscopy and Energy Dispersive X-ray Spectroscopy Measurements

Cross-section polishing of the sintered pellets was performed using an ion milling apparatus (ArBlade5000, Hitachi High-Tech Corporation). During processing, the samples were cooled to −100 °C to prevent thermal damage. The acceleration voltage and discharge voltage were set to 6.0 kV and 1.5 kV, respectively. Scanning electron microscopy (SEM) images (Figures S12−S17) were taken at various magnifications using a SEM (JSM-7800F, JEOL Ltd.) equipped with an energy dispersive X-ray spectroscopy (EDS, X-Max50, Oxford Instruments).

2.5. Theoretical Calculations

Thermodynamic calculations were performed using thermodynamic equilibrium calculation software (FactSage, developed by CRCT and GTT-Technologies) and a thermodynamic database (AIMP ver. 4.0).[7,15] While more recent versions of the AIMP database are available, ver. 4.0 was adopted in this study because it shows better agreement with the experimental results. To simulate the cosintering process in air, the calculations were conducted under open-system conditions, where the partial pressure of oxygen ($p(O_2)$) was fixed at 0.21 atm, reflecting the atmospheric environment. For sintering in an Ar/H_2 atmosphere, the system was modeled considering an equilibrium with a gas phase consisting of 95% Ar and 5% H_2. By fixing the activity of O_2 gas, the software calculates the equilibrium state based on a constant chemical potential. It automatically adds or removes the necessary amount of that gas to maintain the specified partial pressure.

3. RESULTS AND DISCUSSION

3.1. LFP/LATP

3.1.1. LFP/LATP Mixture Sintered in Air. Figure 1a−i shows the XRD patterns, phase composition diagrams obtained by Rietveld analysis, and stable phases predicted by thermodynamic calculations of the LFP, LATP and LFP/LATP mixture before and after sintering at 300−900 °C in air. In addition to the peaks corresponding to the original olivine-type and NASICON-type structures, peaks corresponding to $AlPO_4$ and $Fe_2P_2O_7$ were observed in the LATP and LFP samples, respectively, even before sintering (Figure 1a,c), implying the existence of impurities.

XRD patterns of the LFP sample before and after sintering at 300−900 °C in air (Figure 1a) and phase composition diagrams (Figure 1d) revealed that at 300 °C, most of LFP decomposed into $FePO_4$, Fe_2O_3 and other minor species. This is in reasonable agreement with the thermodynamically predicted phases at 300 °C (Figure 1g), except for the lack of Li_3PO_4. When the temperature was raised to 500 °C, $Li_3Fe_2(PO_4)_3$, Fe_2O_3 and other minor species were detected (Figure 1a,d). The fact that $FePO_4$ was converted to $Li_3Fe_2(PO_4)_3$ suggests that amorphous Li_3PO_4, which is not detectable by XRD, may also be present at 300 °C. After the minor species disappeared at 600 °C from the phase composition diagram (Figure 1d), $Li_3Fe_2(PO_4)_3$ and Fe_2O_3 became dominant with maintaining the composition almost constant within the temperature range of 600 to 900 °C. Unlike, thermodynamic calculations in Figure 1g predicted the formation of Fe_2O_3, $FePO_4$ and Li_3PO_4 at 300−700 °C and Fe_2O_3, $FePO_4$ and $Li_4P_2O_7$ at 800−900 °C. This suggests that the increased temperature activated an alternative reaction pathway leading to $Li_3Fe_2(PO_4)_3$, which remains kinetically trapped due to the substantial energy barrier for further transition. Furthermore, our calculations indicate that the energy difference between the most stable phases ($FePO_4$ and Li_3PO_4 at 300−700 °C and $FePO_4$ and $Li_4P_2O_7$ at 800−900 °C) and the metastable phase $Li_3Fe_2(PO_4)_3$ is marginal and thus the phase selection becomes sensitive to kinetic factors rather than purely thermodynamic stability.

XRD patterns of the LATP sample before and after sintering at 300−900 °C in air (Figure 1c) and phase composition diagrams (Figure 1f) show that LATP after sintering in air retained its structure throughout the temperature range. This result is in good agreement with the predictions by

Downloaded from pubs.acs.org/jpccck/article-pdf/130/37/12864/6809563/acs.jpcc.6c03720.pdf by NATL INST FOR MATLS SCIENCE (NIMS) user on 25 September 2026

https://doi.org/10.1021/acs.jpcc.6c03720
J. Phys. Chem. C 2026, 130, 12864−12874

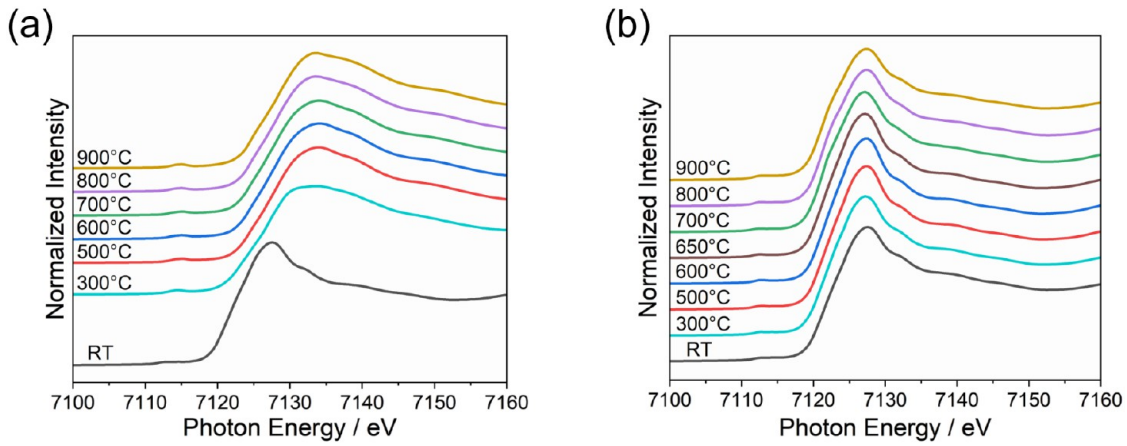


Figure 2. Fe K-edge XANES spectra of LFP/LATP mixtures sintered at various temperatures in (a) air and (b) an Ar/H_2 atmosphere.

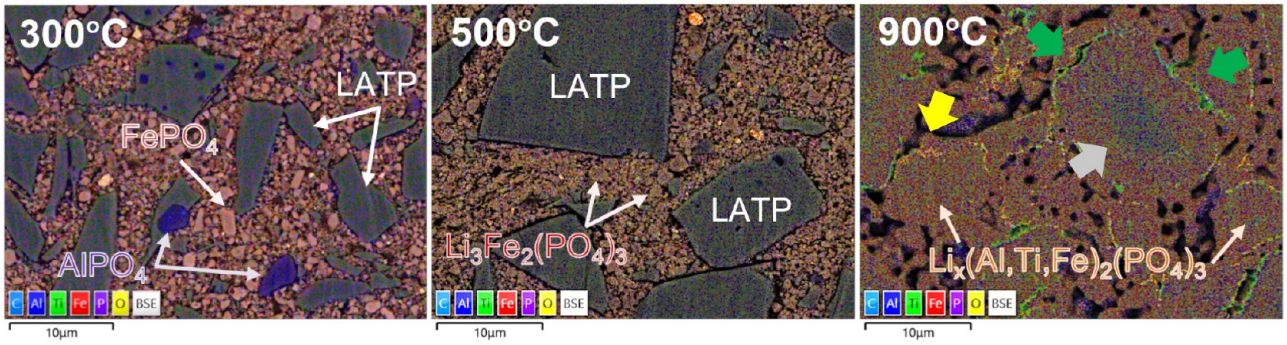


Figure 3. Cross-sectional SEM-EDS elemental maps of LFP/LATP sintered at 300, 500, and 900 °C in air.

thermodynamic calculations (Figure 1i), confirming very high chemical stability of LATP.

XRD patterns of LFP/LATP mixture before and after sintering at 300−900 °C (Figure 1b) and phase composition diagrams (Figure 1e) show that after sintering at 300 °C, LFP in the LFP/LATP mixture was almost completely decomposed into Fe^{3+} compounds such as $FePO_4$ and Fe_2O_3 as is the case of the LFP sample (Figure 1a,d), while LATP and the impurity $Fe_2P_2O_7$ remained. The oxidation of Fe ions is further supported by the shift of the Fe K-edge to the higher energies in the XANES spectra of the LFP/LATP mixtures sintered at 300 °C or above (Figure 2).[16,17] At 500 °C, $FePO_4$ was converted to $Li_3Fe_2(PO_4)_3$ (Figure 1b,e), confirming the formation of energetically competitive metastable phase. The structure of LATP was retained up to 700 °C, but from 800 °C LATP started to decrease together with $Li_3Fe_2(PO_4)_3$ to form a solid solution which has a lattice parameter slightly different from the original LATP. This species is denoted as Fe-rich $Li_x(Al,Ti,Fe)_2(PO_4)_3$ based on the SEM-EDS map (Figure S17) described later. It is worth noting that $Li_3Fe_2(PO_4)_3$ provided the best fit for the Rietveld refinement of Fe-rich $Li_x(Al,Ti,Fe)_2(PO_4)_3$.

In addition to LATP, $FePO_4$ and Fe_2O_3, thermodynamic calculations (Figure 1h) predicted Li_3PO_4 at 300 °C, which was absent in the phase composition diagram (Figure 1e). The lack of Li_3PO_4 can be interpreted by the formation of an amorphous or poorly crystalline lithium-containing phosphate phase, which was presumably consumed with $FePO_4$ at 500 °C to form the energetically competitive phase $Li_3Fe_2(PO_4)_3$ as is the case of the LFP sample (Figure 1d,g). Another significant discrepancy is the prediction of $Li_4P_2O_7$ with remaining LATP, $FePO_4$ and Fe_2O_3 at 800−900 °C (Figure 1h) without forming Fe-rich $Li_x(Al,Ti,Fe)_2(PO_4)_3$ which is the major experimentally identified species (Figure 1e). This discrepancy should be caused by the absence of thermodynamic parameter and crystal structure of Fe-rich $Li_x(Al,Ti,Fe)_2(PO_4)_3$ in the database used in the present study. The absence of Fe-rich $Li_x(Al,Ti,Fe)_2(PO_4)_3$ at 700 °C or lower is likely due to kinetic limitations.

Figures 3 and S12 show SEM-EDS elemental maps of the LFP/LATP mixture sintered at 300, 500, and 900 °C in air. At 300 and 500 °C, LATP and the LFP-derived Fe-containing phases were clearly identified from each other, and elemental composition of each grain was in reasonable agreement with those chemical species detected by XRD. At 900 °C, however, Fe ions were uniformly distributed and the elemental composition was almost identical throughout the cross-section of sintered composite. This confirms that sintering LFP and LATP at 900 °C in air promote the diffusion of Fe ions into LATP, forming the Fe-rich $Li_x(Al,Ti,Fe)_2(PO_4)_3$ phase, as discussed above. Interestingly, a relatively large grain contains a central region with a slightly lower Fe content (gray area indicated by the gray arrow) than surrounding area. Additionally, Ti-rich layers (green area indicated by the green arrows) and O-rich layers (yellow area indicated by the yellow arrow) were formed at the outer surface of several particles. Such nonuniform elemental distribution within the individual particles indicates that the diffusion of Fe ions is relatively slow. Overall, higher sintering temperatures promote further densification and numerous small pores have coalesced into larger voids.

https://doi.org/10.1021/acs.jpcc.6c03720
J. Phys. Chem. C 2026, 130, 12864−12874

Downloaded from pubs.acs.org/jpccck/article-pdf/130/37/12864/6809563/acs.jpcc.6c03720.pdf by NATL INST FOR MATLS SCIENCE (NIMS) user on 25 September 2026

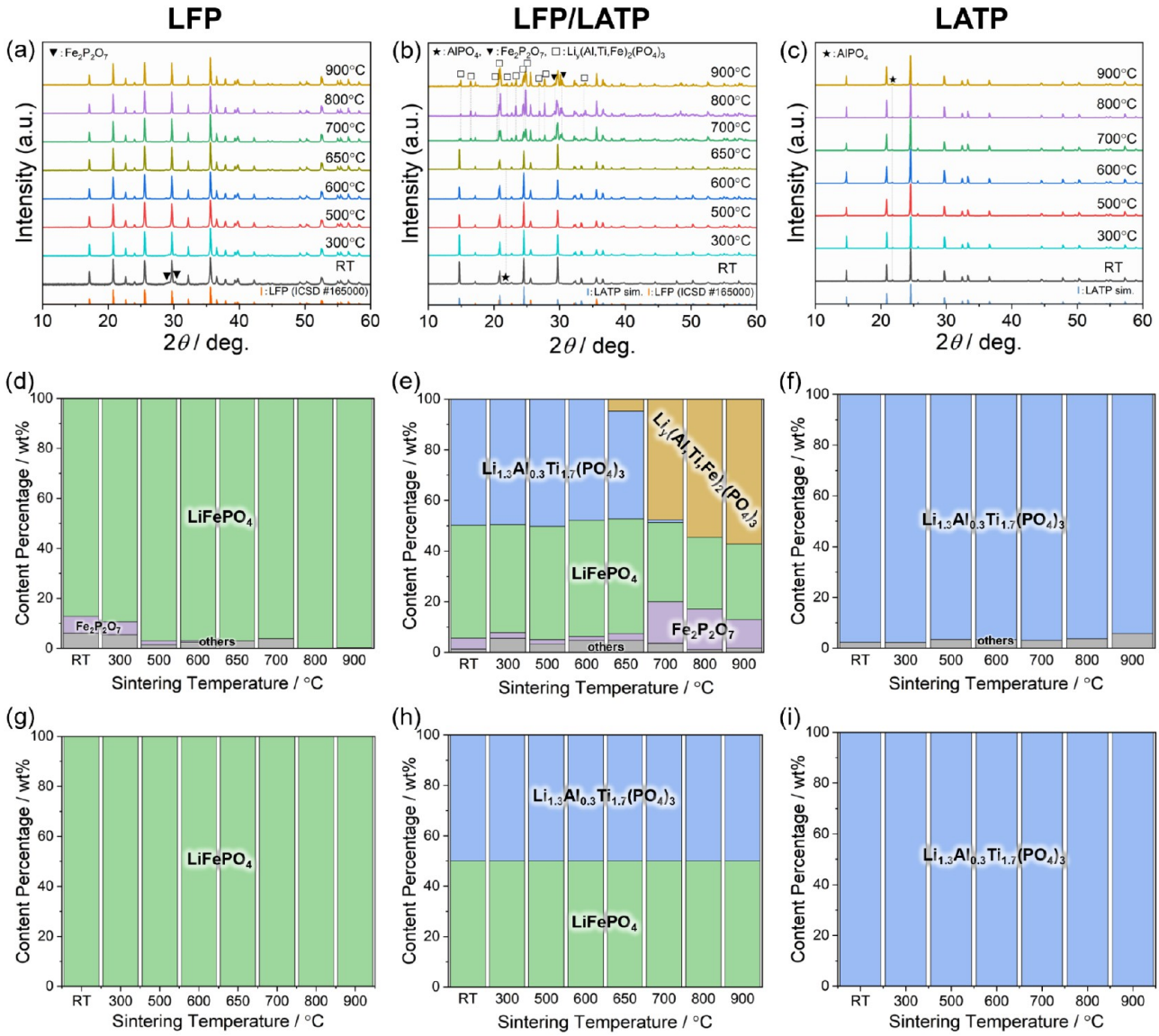


Figure 4. (a–c) XRD patterns and (d–f) phase composition diagrams obtained by Rietveld analysis of (a, d) LFP, (b, e) LFP/LATP and (c, f) LATP sintered at various temperatures in an Ar/H_2 atmosphere. Stable phases predicted by thermodynamic calculations of (g) LFP, (h) LFP/LATP and (i) LATP at various temperatures in an Ar/H_2 atmosphere.

3.1.2. LFP/LATP Mixture Sintered in Ar/H_2. Figure 4a–i shows the XRD patterns, phase composition diagrams obtained by Rietveld analysis, and stable phases predicted by thermodynamic calculations of the LFP, LATP and LFP/LATP mixture before and after sintering at 300–900 °C in an Ar/H_2 atmosphere.

XRD patterns of the LFP sample before and after sintering at 300–900 °C in an Ar/H_2 atmosphere (Figure 4a) and phase composition diagrams (Figure 4d) show that, unlike in air where most of LFP decomposed at 300 °C (Figure 1a,d), LFP retained its crystal structure throughout the temperature range. This is indeed consistent with the thermodynamic calculations for the Ar/H_2 atmosphere (Figure 4g). XRD patterns of the LATP sample before and after sintering at 300–900 °C in an Ar/H_2 atmosphere (Figure 4c) and phase composition diagrams (Figure 4f) show that, although a small amount of $AlPO_4$ was formed, LATP remained unchanged after sintering in the temperature range from 300 to 900 °C, confirming the very high chemical stability of LATP as is the case of sintering in air (Figure 1f). In addition, the results are generally consistent with the predictions from thermodynamic calculations (Figure 4i).

When the LFP/LATP mixture was sintered at temperatures between 300 and 600 °C, the structures and compositions of LFP and LATP remained unchanged from the initial state (Figure 4b,e). At 650 °C, however, the consumption of LATP was accompanied by the formation of a NASICON-type phase with lattice parameters slightly different from those of the original LATP (Figure 4b,e). At 700 °C, LATP was completely transformed into this new NASICON-type phase, while a significant reduction in LFP was observed simultaneously with the formation of $Fe_2P_2O_7$ (Figure 4b,e). This new NASICON-type structure can be assigned to Fe-doped LATP denoted as Fe-poor $Li_y(Al,Ti,Fe)_2(PO_4)_3$ based on the reasonable Rietveld refinement results using $Li_2Ti_2(PO_4)_3$ (Figure 4b) and the SEM-EDS composition analysis (Figure S17). It should be noted that the concentration of Fe ions in this Fe-poor $Li_y(Al,Ti,Fe)_2(PO_4)_3$ is substantially different from that of Fe-

Downloaded from pubs.acs.org/jpccck/article-pdf/130/37/12864/6809563/acs.jpcc.6c03720.pdf by NATL INST FOR MATLS SCIENCE (NIMS) user on 25 September 2026

https://doi.org/10.1021/acs.jpcc.6c03720
J. Phys. Chem. C 2026, 130, 12864–12874

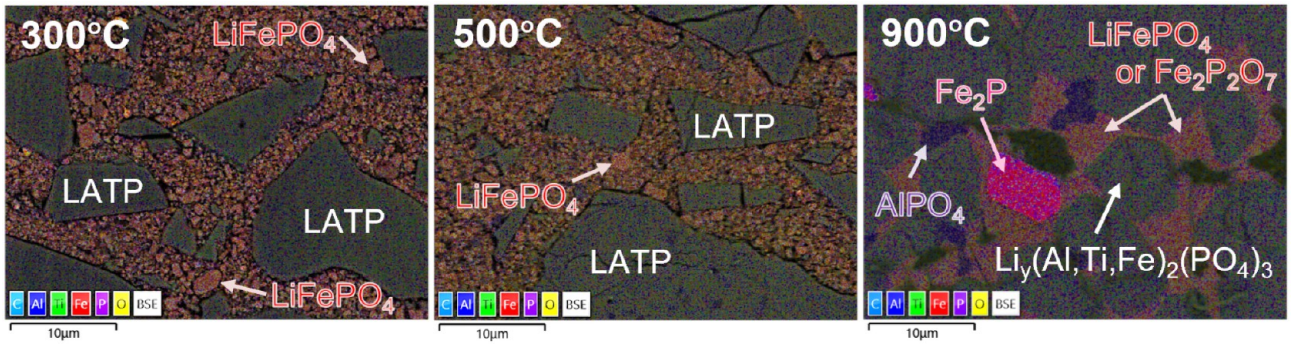


Figure 5. Cross-sectional SEM-EDS elemental maps of LFP/LATP sintered at 300, 500, and 900 °C in an Ar/H_2 atmosphere.

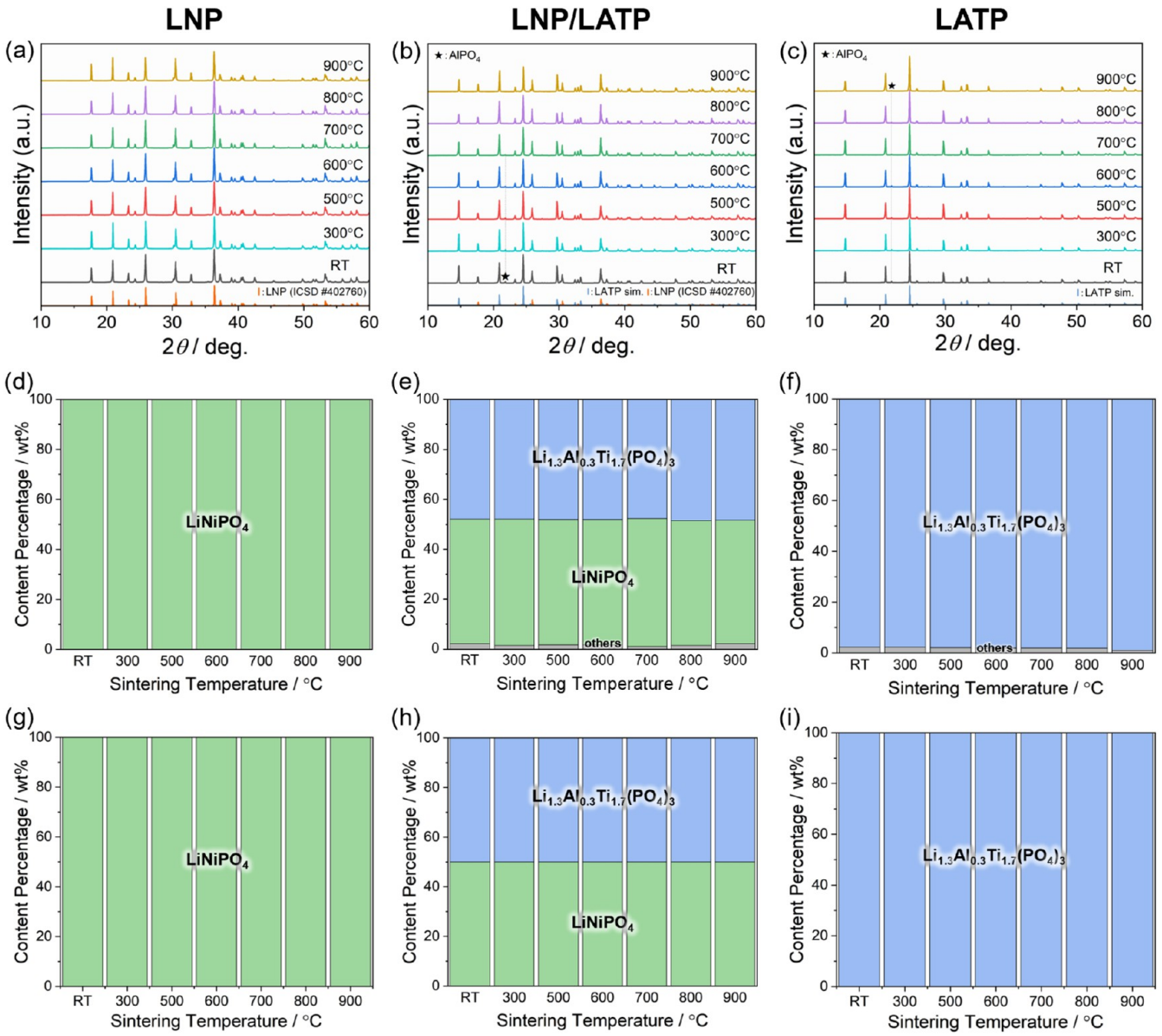


Figure 6. (a–c) XRD patterns and (d–f) phase composition diagrams obtained by Rietveld analysis of (a, d) LNP, (b, e) LNP/LATP and (c, f) LATP sintered at various temperatures in air. Stable phases predicted by thermodynamic calculations of (g) LNP, (h) LNP/LATP and (i) LATP at various temperatures in air.

rich $Li_x(Al,Ti,Fe)_2(PO_4)_3$ which was formed by sintering LFP/LATP mixture at high temperatures (800–900 °C, Figure 1e) in air.

Thermodynamic calculations (Figure 4h) show that LATP and LFP maintained a 1:1 composition throughout the temperature range. The experimentally determined phase

https://doi.org/10.1021/acs.jpcc.6c03720
J. Phys. Chem. C 2026, 130, 12864–12874

Downloaded from pubs.acs.org/jpccck/article-pdf/130/37/12864/6809563/acs.jpcc.6c03720.pdf by NATL INST FOR MATLS SCIENCE (NIMS) user on 25 September 2026

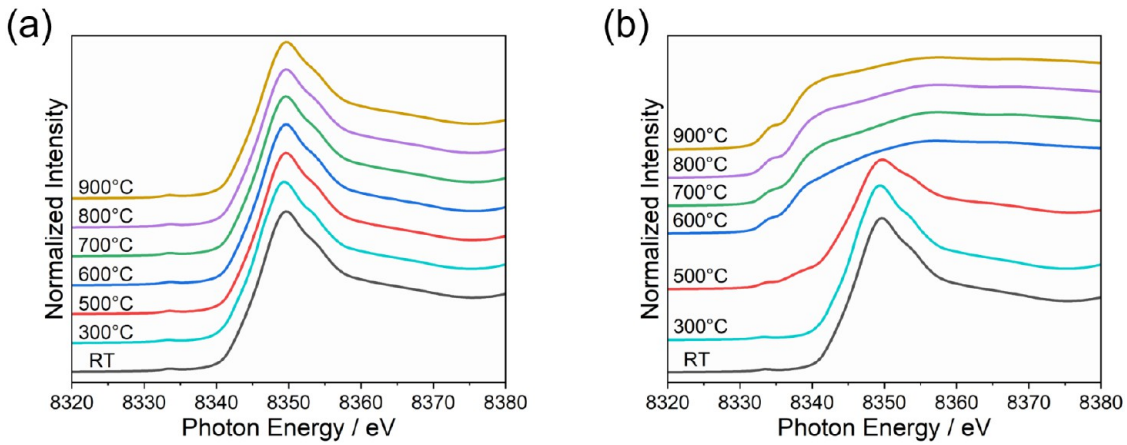


Figure 7. Ni K-edge XANES spectra of LNP/LATP mixtures sintered at various temperatures in (a) air and (b) an Ar/H_2 atmosphere.

compositions and the thermodynamically predicted phase compositions are almost consistent with each other in the temperature range between 300 and 600 °C. However, Fe-poor $Li_y(Al,Ti,Fe)_2(PO_4)_3$ and $Fe_2P_2O_7$ which were observed experimentally at 650 °C and above, were not reproduced by the calculations due to the lack of the thermodynamic parameter and crystal structure of Fe-poor $Li_y(Al,Ti,Fe)_2(PO_4)_3$ in the database.

Figures 5 and S14 show SEM-EDS elemental maps of the LFP/LATP mixture sintered at 300, 500, and 900 °C in an Ar/H_2 atmosphere. After sintering at 300 and 500 °C, only the grains which have identical elemental compositions to those of LATP and LFP were observed, confirming both XRD results and theoretical predictions. In addition, $Fe_2P_2O_7$, LFP and Fe-poor $Li_y(Al,Ti,Fe)_2(PO_4)_3$ were clearly imaged after sintering at 900 °C as well as a few minor species such as iron phosphides Fe_2P (dark magenta area) and $AlPO_4$ (dark purple area). Note that no peak derived from Fe_2P was observed in XRD because of its extremely small content or amorphous structure.[18−21] Consistent with the previous results, densification further progressed at higher sintering temperatures.

3.2. LNP/LATP

3.2.1. LNP/LATP Mixture Sintered in Air. Figure 6a−i shows the XRD patterns, phase composition diagrams obtained by Rietveld analysis, and stable phases predicted by thermodynamic calculations of the LNP, LATP and LNP/LATP mixture before and after sintering at 300−900 °C in air. All of the experimental data and theoretical predictions in Figure 6a−i show that the structures of both LATP and LNP alone were retained after sintering in this temperature range, and the experimental results were completely consistent with the thermodynamically predicted phases. Furthermore, unlike the LFP/LATP mixture sintered in air, the structures and compositions of both materials were also maintained in the LNP/LATP mixture, which was well reproduced by thermodynamic calculations Figure 6h.

Figures 8 and S15 show SEM-EDS elemental maps of the LNP/LATP mixture sintered at 300, 500, and 900 °C in air. The growth and densification of each grain can be observed with increasing sintering temperature, while their elemental compositions are maintained. The map at 900 °C shows a Ti-rich, Al-poor phase (dark green area) with a composition close to that of LATP. This suggests that the majority of LNP and LATP retained their crystal structures, while the diffusion of Ti and Al ions occurred.

3.2.2. LNP/LATP Mixture Sintered in Ar/H_2. Figure 9a−i shows the XRD patterns, phase composition diagrams obtained by Rietveld analysis, and stable phases predicted by thermodynamic calculations of the LNP, LATP and LNP/LATP mixture before and after sintering at 300−900 °C in an Ar/H_2 atmosphere.

Dramatic changes in XRD patterns and phase compositions were observed for both LNP sample (Figure 9a,d) and LNP/LATP mixture (Figure 9b,e) after sintering in an Ar/H_2 atmosphere. LNP decomposed to form a variety of reaction products after sintering the LNP sample and LNP/LATP mixture, and resulting products were completely inconsistent with stable phases predicted by thermodynamic calculations as shown in Figure 9g and h. In the case of the LNP sample, LNP decomposed to nickel phosphides such as $Ni_{12}P_5$ and Ni_2P and pyrophosphates such as $Li_4P_2O_7$ and $Li_2Ni_2(P_2O_7)_2$ (Figure 9a,d) whereas thermodynamic calculations predicted the formation of $LiPH_2O_4$, $LiPO_3$, metallic Ni and H_2O (Figure 9g). Moreover, in the case of LNP/LATP mixture, first LNP decomposed alone at 500 °C to form $Ni_{12}P_5$ and Ni_2P (Figure 9b,e) as is the case of the LNP sample (Figure 9a,d), and then LATP was involved in the reaction to form NASICON-type phases with lattice parameters slightly different from those of the original LATP at 700 °C or higher (Figure 9b,e). SEM-EDS elemental map of the LNP/LATP mixture sintered at 900 °C (Figure S17d) revealed the existence of Ni-doped and Ni-free LATP like domains and their nonuniform chemical compositions across the sample. Despite the variations in local chemical composition indicated by SEM-EDS maps, the Rietveld refinement of the newly observed NASICON-type phase was performed based on the structural model of $Li_2Ti_2(PO_4)_3$, as it provided the best fit for the overall diffraction profile. The NASICON-type species with various local stoichiometries are collectively referred to as $Li_z(Al,Ti,Ni)_2(PO_4)_3$ in Figure 9e and thereafter.

As with the LNP sample (Figure 9g), thermodynamic calculations for the LNP/LATP mixtures after sintering (Figure 9h) did not well-reproduce the reaction products. Ni compounds are readily reduced under a reducing atmosphere,[20] and the release of oxygen occurred associated with the reduction of divalent Ni ions in LNP to zerovalent Ni in $Ni_{12}P_5$ and Ni_2P. In fact, the shift of the Ni K-edge to the lower energies was clearly observed in the XANES spectra of the LNP/LATP mixtures sintered at 600 °C or above (Figure 7b),

https://doi.org/10.1021/acs.jpcc.6c03720
J. Phys. Chem. C 2026, 130, 12864−12874

Downloaded from pubs.acs.org/jpccck/article-pdf/130/37/12864/6809563/acs.jpcc.6c03720.pdf by NATL INST FOR MATLS SCIENCE (NIMS) user on 25 September 2026

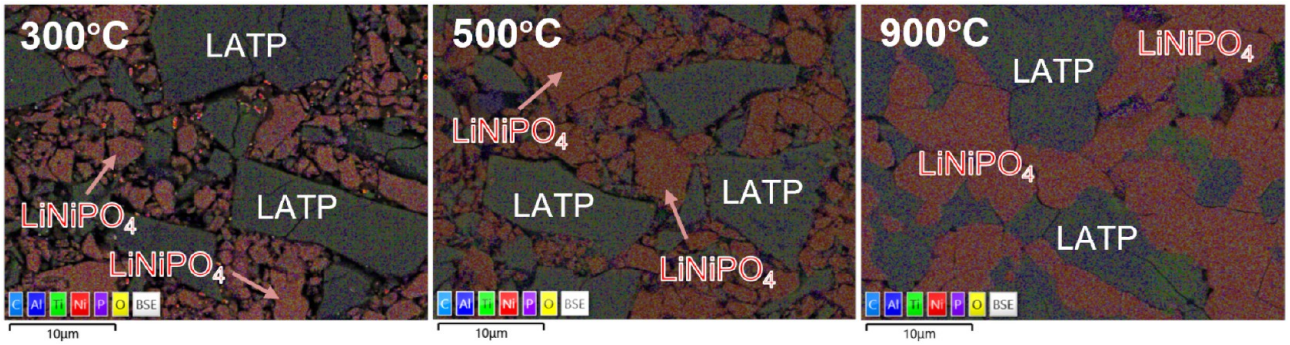


Figure 8. Cross-sectional SEM-EDS elemental maps of LNP/LATP sintered at 300, 500, and 900 °C in air.

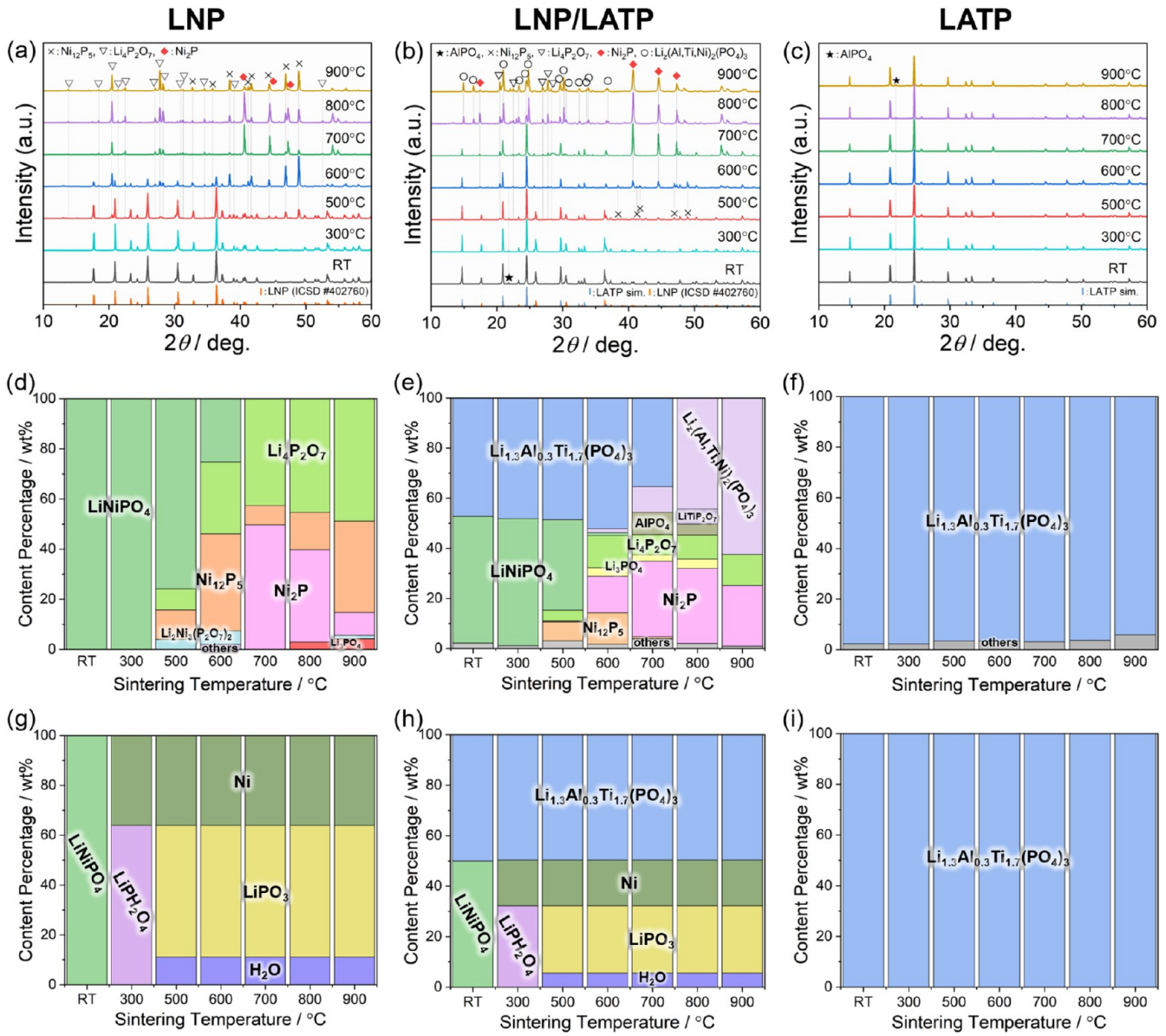


Figure 9. (a–c) XRD patterns and (d–f) phase composition diagrams obtained by Rietveld analysis of (a, d) LNP, (b, e) LNP/LATP and (c, f) LATP sintered at various temperatures in an Ar/H_2 atmosphere. Stable phases predicted by thermodynamic calculations of (g) LNP, (h) LNP/LATP and (i) LATP at various temperatures in an Ar/H_2 atmosphere.

confirming the formation of Ni_2P which is a prominent species in XRD.

Thus, due to the release of oxygen accompanying the reduction of Ni ions, the thermodynamic calculations in Figure 9h cannot accurately reproduce the experimental results at any

https://doi.org/10.1021/acs.jpcc.6c03720
J. Phys. Chem. C 2026, 130, 12864−12874

Downloaded from pubs.acs.org/jpccck/article-pdf/130/37/12864/6809563/acs.jpcc.6c03720.pdf by NATL INST FOR MATLS SCIENCE (NIMS) user on 25 September 2026

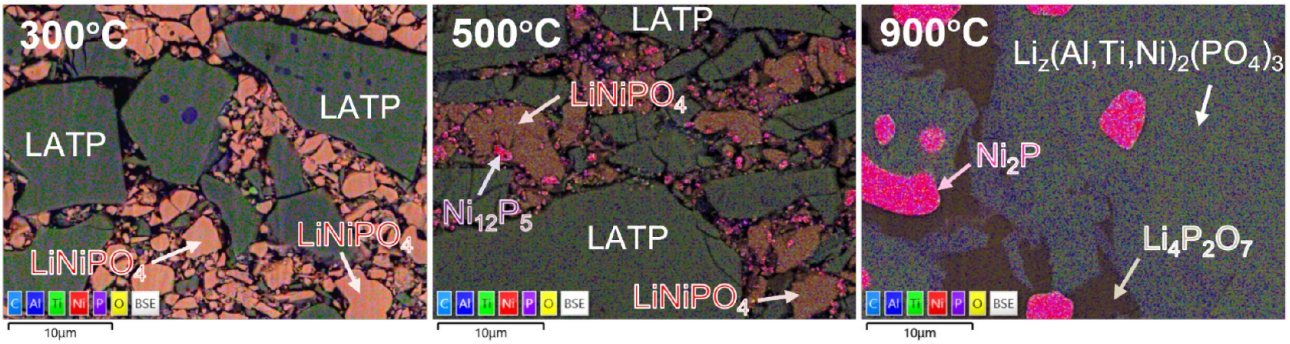


Figure 10. Cross-sectional SEM-EDS elemental maps of LNP/LATP sintered at 300, 500, and 900 °C in an Ar/H_2 atmosphere.

temperature. Furthermore, the thermodynamic data for nickel phosphides in the AIMP database should be treated with caution. The AIMP database is primarily based on the Materials Project,[22] which includes ab initio calculation data and experimental data. However, it contains very few calculated entries for the Ni−P system. Consequently, the AIMP database relies almost exclusively on experimental data for these compounds. This is problematic because experimental data for phosphides are often unreliable and inconsistent, largely due to difficulties in synthesis and characterization caused by the high volatility of phosphorus.

Figures 10 and S16 show SEM-EDS elemental maps of the LNP/LATP mixture sintered at 300, 500, and 900 °C in an Ar/H_2 atmosphere. When sintered at 500 °C, the decomposition of LNP was confirmed to result in the formation of Ni phosphides (magenta area) such as $Ni_{12}P_5$. At 900 °C, LNP completely disappeared, and Ni phosphides (magenta area) such as Ni_2P became the main product together with $Li_z(Al,Ti,Ni)_2(PO_4)_3$.

In this study, the effects of material combinations and the sintering atmosphere were systematically investigated by classifying the experiments into four distinct conditions: LFP/LATP in air, LFP/LATP in Ar/H_2, LNP/LATP in air, and LNP/LATP in Ar/H_2. With the exception of LNP/LATP in air, for which no reaction was observed, the corresponding reaction equations for each system are provided in the Supporting Information.

The Fe ions in LFP are originally divalent (Fe^{2+}) with an ionic radius of 0.78 Å.[23] Under a reducing atmosphere, the divalent state is retained during sintering (Figure 2b), whereas, in an oxidizing atmosphere, the Fe ions are oxidized to the trivalent state (Fe^{3+}) at every temperature examined in the present study (300−900 °C) (Figure 2a), and the ionic radius becomes 0.645 Å.[23] When Fe ions are incorporated into the LATP lattice, the Ti^{4+} and Al^{3+} sites of LATP are considered the principal substitution sites. Because the size of Fe^{3+} (0.645 Å) is close to that of Ti^{4+} (0.605 Å) and Al^{3+} (0.535 Å),[23] Fe-rich LATP forms under oxidizing conditions (Figure 1 and Figure S17b). In contrast, Fe^{2+} differs more markedly in size from Ti^{4+} or Al^{3+} and also carries a different charge. Consequently, under a reducing atmosphere, Fe-poor LATP is expected to form (Figure 4 and Figure S17c).

In the LNP/LATP system, the Ni ions are initially divalent (Ni^{2+}) with an ionic radius of 0.69 Å.[23] In an oxidizing atmosphere, this divalent state is preserved (Figure 7a). The radius is relatively close to those of Ti^{4+} and Al^{3+}, but the charge mismatch makes substitution, diffusion and reaction between the two phases less favorable. Under a reducing atmosphere, Ni are almost completely reduced to a zerovalent species (Figure 7b). As described above, at temperatures of 700 °C or higher, a variety of NASICON-type phases appear (Figure 9). Because some of these phases contain Ni as evident by SEM-EDS (Figure S17d), we collectively denote them as $Li_z(Al,Ti,Ni)_2(PO_4)_3$. It is possible that a small amount of Ni remains unreduced and substitutes for the metal sites in LATP, or that zerovalent Ni species adsorb onto Ni-free NASICON phases instead of ion-substitutions. Thus, the redox susceptibility of the metal ions in a given atmosphere, as well as their ionic size mismatch, governs the cosintering behavior of the LFP/LATP and LNP/LATP systems.

Fe-rich $Li_x(Al,Ti,Fe)_2(PO_4)_3$, Fe-poor $Li_y(Al,Ti,Fe)_2(PO_4)_3$, and $Li_z(Al,Ti,Ni)_2(PO_4)_3$ are presumed not to consist a single, uniform composition, but rather of several phases with similar structures and varying compositions. As a result, the diffraction peaks associated with these multiple phases are overlapped with each other. Therefore, it is difficult to provide a detailed description of their lattice parameters and compositions.

Notably, the initial impurities (see Microstructures and phase compositions of LFP, LNP and LATP powders in the Supporting Information) do not significantly affect the reaction, as the major impurity species, such as $AlPO_4$ and $Fe_2P_2O_7$, remain present even after sintering at 900 °C (Figures 1, 4, 6, and 9), where the reaction is expected to be most active. Indeed, the experimental results in Figure 6 are in reasonable agreement with the calculations. Furthermore, the discrepancies observed in Figures 1 and 4 can be attributed to the formation of phases not registered in the database, as well as to kinetic limitations. Similarly, the difference between the calculated and experimental results in Figure 9 can be interpreted as a result of mass transfer between the system and the surrounding gas phase.

According to the results presented in Figures S12−S17, the influence of particle size was found to be particularly pronounced in the LFP/LATP in air system. Specifically, Figures S12c and S17b demonstrate that, following sintering at 900 °C, Fe diffused broadly throughout the sample except for the central regions of large particles presumed to originate from LATP, where Fe diffusion was not observed. Point analyses performed by EDS indicated that these regions were rich in Ti and preserved a composition close to that of the original LATP. The compositional heterogeneity observed within individual particles is considered to arise from kinetic constraints, such as slow ion diffusion.[7] Nevertheless, as shown in Figure S13, extending the sintering time from 8 to 48 h using the same raw material powders did not result in significant changes in the elemental distribution inside the

https://doi.org/10.1021/acs.jpcc.6c03720
J. Phys. Chem. C 2026, 130, 12864−12874

Downloaded from pubs.acs.org/jpccck/article-pdf/130/37/12864/6809563/acs.jpcc.6c03720.pdf by NATL INST FOR MATLS SCIENCE (NIMS) user on 25 September 2026

particles. Therefore, it is possible that the coexistence of these two phases is thermodynamically stable under the investigated conditions.

Here, we derive practical cosintering guidelines. A fundamental premise is that densification and joining of oxide-based solid electrolytes and electrode materials generally require high temperatures. This tendency was also confirmed by the SEM observations in the present work. For the LFP/LATP system, sintering under a reducing atmosphere (Ar/H_2; Figure 4) is recommended to prevent the oxidation of Fe ions, which otherwise triggers undesired side reactions (Figure 1). Nevertheless, structural changes due to the side reaction of LATP and LFP were observed above 650 °C even in Ar/H_2 atmosphere (Figure 4). Consequently, the preferable cosintering temperature window is 600−650 °C under Ar/H_2 atmosphere, where side reactions are negligible. If higher temperatures are required, the H_2 partial pressure should be lowered. For LNP/LATP system, an oxidizing atmosphere (air; Figure 6) is more favorable because Ni ions are easily reduced in a reducing atmosphere, leading to a variety of unwanted products (Figure 9). Complete densification and the successful LNP/LATP interface formation were confirmed after sintering at 900 °C in air (Figures 6 and 7). These results indicate that when designing cosintering conditions, it is essential to identify the atmosphere-temperature window in which the metal ions of each constituent remain chemically stable.

When the phases predicted by calculations and those observed experiment are not consistent, potential causes include (1) insufficient accuracy of the thermodynamic model or of the Gibbs energy description, and (2) the experimental observation of metastable or kinetically stabilized nonequilibrium phases.[7] Even the extensive ab initio Materials Project database[15] does not contain many minor species that appear in our study, such as Fe-rich $Li_x(Al,Ti,Fe)_2(PO_4)_3$ and Fe-poor $Li_y(Al,Ti,Fe)_2(PO_4)_3$. Consequently, these phases cannot be predicted computationally when they form during experimental cosintering, highlighting the need for continual enrichment of the database. Moreover, a complete and accurate thermodynamic database does not guarantee agreement with experiment because the system may not reach equilibrium within the finite experimental time, resulting in metastable phases. Therefore, when thermodynamic calculations are employed as a screening tool to assess whether cosintering is feasible for a given system and to identify optimal cosintering conditions, it is necessary to consider not only the most stable compound combination but also the second- and third-most stable candidates, which may correspond to metastable phases.

Rather than attributing the discrepancies solely to limited experimental duration, we propose evaluating the free-energy difference (ΔG) between the experimentally observed phase combination and the calculated equilibrium state. Because actual battery materials must endure long-term operation, it is essential to assess whether the phase state obtained by cosintering processes remain unchanged during device use. For example, when the experimentally observed phases coincide with the thermodynamic equilibrium states, i.e., ΔG is small, there is little thermodynamic driving force for a phase transformation, the structure is relatively stable, and a long lifetime can be expected. Conversely, a large ΔG indicates a strong driving force for phase change, which may lead to degradation of device. Thus, thermodynamic calculations are expected to serve not only as a screening tool for sintering conditions but also to yield insights into the long-term stability of the resulting meta-material.

4. CONCLUSION

The reaction products of LFP/LATP and LNP/LATP mixtures sintered at various temperatures under both oxidative and reductive atmospheres were analyzed using various techniques such as XRD, XAFS, and SEM-EDS. In the LFP/LATP mixtures, LFP was oxidized in air to produce Fe^{3+} compounds such as $FePO_4$ and Fe_2O_3 at 300 °C. At 500 °C, $FePO_4$ further reacted with an amorphous or poorly crystalline lithium-containing phosphate phase to form energetically competitive phase $Li_3Fe_2(PO_4)_3$. At temperatures above 700 °C, the Fe-containing products further reacted with LATP to produce Fe-rich $Li_x(Al,Ti,Fe)_2(PO_4)_3$. In an Ar/H_2 atmosphere, LFP and LATP retained 1:1 composition, identical to that before sintering, up to 600 °C. At 650 °C or higher, however, (part of) LFP reacted with LATP to produce $Fe_2P_2O_7$ and Fe-poor $Li_y(Al,Ti,Fe)_2(PO_4)_3$. On the other hand, the composition of LNP/LATP mixture did not change after sintering in air, but in an Ar/H_2 atmosphere, LNP decomposed to produce various phases including Ni phosphides and $Li_z(Al,Ti,Ni)_2(PO_4)_3$.

The cosintering of LFP/LATP and LNP/LATP is significantly affected by the distinct redox behaviors of Fe and Ni, necessitating tailored sintering atmospheres and temperature windows for various olivine-type cathode materials. Moreover, LATP exhibits limited inertness at elevated temperatures and can actively participate in the formation of complex phases derived from the NASICON structure. The products predicted by thermodynamic calculations did not always match the experimental products, and it was suggested that the challenges to predicting experimental results with higher accuracy include (1) expanding the thermodynamic parameters of reference materials in the database (2) considering the energetically competitive species and kinetically trapped metastable phases and (3) taking into account the release of gas components such as water and oxygen.

■ ASSOCIATED CONTENT

Supporting Information

The Supporting Information is available free of charge at https://pubs.acs.org/doi/10.1021/acs.jpcc.6c03720.

Microstructures and phase compositions of LFP, LNP, and LATP powders; details of Rietveld analyses of XRD patterns; cross-sectional SEM images of LFP/LATP and LNP/LATP sintered at various temperatures; determination of compositions of Fe-rich $Li_x(Al,Ti,Fe)_2(PO_4)_3$, Fe-poor $Li_y(Al,Ti,Fe)_2(PO_4)_3$ and $Li_z(Al,Ti,Ni)_2(PO_4)_3$; reaction equations (DOCX)

■ AUTHOR INFORMATION

Corresponding Author

Takuya Masuda − *Research Center for Energy and Environmental Materials (GREEN), National Institute for Materials Science (NIMS), Tsukuba, Ibaraki 305-0044, Japan; Graduate School of Chemical Sciences and Engineering, Hokkaido University, Sapporo, Hokkaido 060-*

Downloaded from pubs.acs.org/jpccck/article-pdf/130/37/12864/6809563/acs.jpcc.6c03720.pdf by NATL INST FOR MATLS SCIENCE (NIMS) user on 25 September 2026

https://doi.org/10.1021/acs.jpcc.6c03720
J. Phys. Chem. C 2026, 130, 12864−12874

*0810, Japan; orcid.org/0000-0001-7462-2177; Email: MASUDA.Takuya@nims.go.jp

Authors

Shuhei Kobayashi − *Research Center for Energy and Environmental Materials (GREEN), National Institute for Materials Science (NIMS), Tsukuba, Ibaraki 305-0044, Japan; Graduate School of Chemical Sciences and Engineering, Hokkaido University, Sapporo, Hokkaido 060-0810, Japan*

Kei Kubota − *Research Center for Energy and Environmental Materials (GREEN), National Institute for Materials Science (NIMS), Tsukuba, Ibaraki 305-0044, Japan; Graduate School of Chemical Sciences and Engineering, Hokkaido University, Sapporo, Hokkaido 060-0810, Japan; orcid.org/0000-0001-8941-3650*

Fumihiko Ichihara − *Research Center for Energy and Environmental Materials (GREEN), National Institute for Materials Science (NIMS), Tsukuba, Ibaraki 305-0044, Japan; orcid.org/0000-0002-0274-1342*

Machiko Ode − *Research Center for Structural Materials, National Institute for Materials Science (NIMS), Tsukuba, Ibaraki 305-0047, Japan*

Shogo Miyoshi − *Research Center for Energy and Environmental Materials (GREEN), National Institute for Materials Science (NIMS), Tsukuba, Ibaraki 305-0044, Japan; orcid.org/0000-0003-0375-1187*

Complete contact information is available at: https://pubs.acs.org/10.1021/acs.jpcc.6c03720

Notes

The authors declare no competing financial interest.

■ ACKNOWLEDGMENTS

The authors would like to acknowledge the financial support provided by the Materials Processing Science project "Materealize" of the Ministry of Education, Culture, Sports, Science and Technology of Japan (MEXT; grant no. JPMXP0219207397). The synchrotron radiation experiments were carried out as a certified project of the High Energy Accelerator Research Organization (KEK) (proposal no. 2023G131).

■ REFERENCES

(1) Chen, R.; Li, Q.; Yu, X.; Chen, L.; Li, H. Approaching Practically Accessible Solid-State Batteries: Stability Issues Related to Solid Electrolytes and Interfaces. *Chem. Rev.* **2020**, *120* (14), 6820−6877.

(2) Kim, K. J.; Rupp, J. L. M. All ceramic cathode composite design and manufacturing towards low interfacial resistance for garnet-based solid-state lithium batteries. *Energy Environ. Sci.* **2020**, *13* (12), 4930−4945.

(3) Gellert, M.; Dashjav, E.; Grüner, D.; Ma, Q.; Tietz, F. Compatibility study of oxide and olivine cathode materials with lithium aluminum titanium phosphate. *Ionics* **2018**, *24* (4), 1001−1006.

(4) Yu, C.-Y.; Choi, J.; Anandan, V.; Kim, J.-H. High-Temperature Chemical Stability of $Li_{1.4}Al_{0.4}Ti_{1.6}(PO_4)_3$ Solid Electrolyte with Various Cathode Materials for Solid-State Batteries. *J. Phys. Chem. C* **2020**, *124* (28), 14963−14971.

(5) Ichihara, F.; Miyoshi, S.; Masuda, T. Co-sintering process of $LiCoO_2$ cathodes and NASICON-type LATP solid electrolytes studied by X-ray diffraction and X-ray absorption near edge structure. *Phys. Chem. Chem. Phys.* **2022**, *24* (42), 25878−25884.

(6) Beaupain, J. P.; Waetzig, K.; Otto, S. K.; Henss, A.; Janek, J.; Malaki, M.; Pokle, A.; Muller, J.; Butz, B.; Volz, K.; Kusnezoff, M.; Michaelis, A. Reaction of $Li_{1.3}Al_{0.3}Ti_{1.7}(PO_4)_3$ and $LiNi_{0.6}Co_{0.2}Mn_{0.2}O_2$ in Co-Sintered Composite Cathodes for Solid-State Batteries. *ACS Appl. Mater. Interfaces* **2021**, *13* (40), 47488−47498.

(7) Ichihara, F.; Miyoshi, S.; Ode, M.; Masuda, T. Co-sintering Reaction Analysis of $LiCoO_2$ Cathodes and NASICON-Type LATP Solid Electrolytes Studied by Experimental and Computational Methods. *J. Phys. Chem. C* **2025**, *129* (28), 12738−12749.

(8) Ichihara, F.; Niitsu, K.; Tanaka, Y.; Niwa, Y.; Mitsuishi, K.; Miyoshi, S.; Ohno, T.; Masuda, T. Structural Analysis of the $LiCoPO_4$ Electrode/NASICON-Type $Li_{1.3}Al_{0.3}Ti_{1.7}(PO_4)_3$ Solid Electrolyte Interface. *J. Phys. Chem. C* **2023**, *127* (31), 15043−15050.

(9) Saunders, N.; Miodownik, A. P. *CALPHAD: Calculation of phase diagrams: A comprehensive guide*; Pergamon, 1998.

(10) Lukas, H.; Fries, S. G.; Sundman, B. *Computational Thermodynamics*; Cambridge University Press, 2007. DOI:

(11) Niitsu, K.; Ichihara, F.; Miyoshi, S.; Ode, M.; Mitsuishi, K.; Masuda, T.; Takada, K. Structural analysis of the $LiCoO_2$ cathodes/garnet-type $Li_{6.5}La_3Zr_{1.5}Ta_{0.5}O_{12}$ solid electrolyte interface. *Solid State Ionics* **2025**, *421*, 116804.

(12) Liu, F.; He, H.; Lian, Z.; Shan, W.; Xie, L.; Asakura, K.; Yang, W.; Deng, H. Highly dispersed iron vanadate catalyst supported on TiO_2 for the selective catalytic reduction of NO_x with NH_3. *J. Catal.* **2013**, *307*, 340−351.

(13) Abe, H.; Niwa, Y.; Kimura, M. A surface sensitive hard X-ray spectroscopic method applied to observe the surface layer reduction reaction of Co oxide to Co metal. *Phys. Chem. Chem. Phys.* **2020**, *22* (43), 24974−24977.

(14) Ravel, B.; Newville, M. ATHENA and ARTEMIS: Interactive Graphical Data Analysis using IFEFFIT. *Phys. Scr.* **2005**, *T115*, 1007−1010.

(15) Ong, S. P.; Richards, W. D.; Jain, A.; Hautier, G.; Kocher, M.; Cholia, S.; Gunter, D.; Chevrier, V. L.; Persson, K. A.; Ceder, G. Python Materials Genomics (pymatgen): A robust, open-source python library for materials analysis. *Comput. Mater. Sci.* **2013**, *68*, 314−319.

(16) Liu, J.; Xiao, B.; Banis, M. N.; Li, R.; Sham, T.-K.; Sun, X. Atomic layer deposition of amorphous iron phosphates on carbon nanotubes as cathode materials for lithium-ion batteries. *Electrochim. Acta* **2015**, *162*, 275−281.

(17) Prince, A. A. M.; Mylswamy, S.; Chan, T. S.; Liu, R. S.; Hannoyer, B.; Jean, M.; Shen, C. H.; Huang, S. M.; Lee, J. F.; Wang, G. X. Investigation of Fe valence in $LiFePO_4$ by Mössbauer and XANES spectroscopic techniques. *Solid State Commun.* **2004**, *132* (7), 455−458.

(18) Trudeau, M. L.; Laul, D.; Veillette, R.; Serventi, A. M.; Mauger, A.; Julien, C. M.; Zaghib, K. In situ high-resolution transmission electron microscopy synthesis observation of nanostructured carbon coated $LiFePO_4$. *J. Power Sources* **2011**, *196* (18), 7383−7394.

(19) Liu, Y.; Liu, J.; Wang, J.; Banis, M. N.; Xiao, B.; Lushington, A.; Xiao, W.; Li, R.; Sham, T. K.; Liang, G.; Sun, X. Formation of size-dependent and conductive phase on lithium iron phosphate during carbon coating. *Nat. Commun.* **2018**, *9* (1), 929.

(20) Herle, P. S.; Ellis, B.; Coombs, N.; Nazar, L. F. Nano-network electronic conduction in iron and nickel olivine phosphates. *Nat. Mater.* **2004**, *3* (3), 147−152.

(21) Kang, B.; Ceder, G. Battery materials for ultrafast charging and discharging. *Nature* **2009**, *458* (7235), 190−193.

(22) Jain, A.; Ong, S. P.; Hautier, G.; Chen, W.; Richards, W. D.; Dacek, S.; Cholia, S.; Gunter, D.; Skinner, D.; Ceder, G.; et al. Commentary: The Materials Project: A materials genome approach to accelerating materials innovation. *APL Mater.* **2013**, *1* (1), 011002.

(23) Shannon, R. Revised effective ionic radii and systematic studies of interatomic distances in halides and chalcogenides. *Acta Crystallogr.* **1976**, *32* (5), 751−767.

Downloaded from pubs.acs.org/jpccck/article-pdf/130/37/12864/6809563/acs.jpcc.6c03720.pdf by NATL INST FOR MATLS SCIENCE (NIMS) user on 25 September 2026